EUROPEAN FUSION DEVELOPMENT AGREEMENT

EFDA–JET–PR(04)36

I. Furno , H. Weisen, C. Carey, C. Angioni R. Behn, E. Fable,A. Zabolotski,
the TCV Team and JET EFDA contributors

A New Method for the Inversion of Interferometry Data using Basis Functions Derived from Singular Value Decomposition of Local Measurements in Tokamak Plasmas

A New Method for the Inversion of Interferometry Data using Basis Functions Derived from Singular Value Decomposition of Local Measurements in Tokamak Plasmas

I. Furno[1], H. Weisen[2], C. Carey[1], C. Angioni[3], R. Behn[2], E. Fable[2], A. Zabolotski[2], the TCV Team[2] and JET EFDA contributors*

[1]Los Alamos National Laboratory, M.S. E526, Los Alamos, NM 87545, USA
[2]Centre de Recherches en Physique des Plasmas, Association Euratom-Confédération Suisse, EPFL, Lausanne, Switzerland
[3]Max-Planck-Institut für Plasmaphysik, IPP-EURATOM Association, D-85748 Garching bei München, Germany
** See annex of J. Pamela et al, "Overview of Recent JET Results and Future Perspectives", Fusion Energy 2002 (Proc. 19th IAEAFusion Energy Conference, Lyon (2002)).*

Preprint of Paper to be submitted for publication in
Plasma Physics and Controlled Fusion

ABSTRACT

A novel method for inverting time-resolved line integrated interferometric plasma density measurements is described. The method uses singular value decomposition of local density profiles from Thomson scattering measurements obtained at low sampling rates in the same or equivalent plasmas to determine a set of orthogonal spatial basis functions which is well adapted to the physical processes under investigation. The sought-for density profile is expanded into a limited series of these functions and a solution is calculated by using a simple least-square fit method.

The new method overcomes the difficulties encounter with other methods, such as regularization methods, which smoothen gradients and depend on the availability of accurate measurements in plasma edge region. The small number of computations required provides for a fast algorithm. This method, which combines the high bandwidth of interferometer systems with the spatial accuracy of Thomson scattering, is applied to invert interferometer measurements in a wide variety of operational regimes in the TCV and JET tokamaks. In particular, the collisionality dependence of density peaking observed in ASDEX Upgrade is confirmed in JET H-modes using this method.

1. INTRODUCTION

Understanding and control of particle transport is an important issue for thermonuclear fusion research since it determines the transport of the reactants and reaction products towards and away from the core of the plasma. Particle transport studies in plasmas require measurements of density profiles with high temporal and spatial resolution. In fusion research devices, two different diagnostics are commonly used to perform these measurements. Interferometer systems provide line integrated density measurements with high temporal resolution from the phase shift of a laser beam across the plasma cross section. Thomson scattering systems provide local density measurements by detecting the scattered laser light from a small volume of plasma. Although Thomson scattering systems have the advantage of providing local density profiles, their time resolution is limited by the repetition rate of the laser system and is usually inadequate for resolving fast transport phenomena. In contrast, interferometer systems have high sampling rates allowing fast changes of the line-integrated density to be measured. However, because they are line-integrated they require solving an inverse problem for calculating the local density profile. Due to access limitations in tokamak devices, interferometer systems with a single fan of probing beams are the practical choice [1], [2], [3], [4]. In this case, additional information about the structure of the electron density is required to solve the inverse problem. One possibility is to require the solution to satisfy some constraints. The Minimum Fisher Information (MFI) is particularly successful in inverting line-integrated interferometric data [2] by minimizing the Fisher Information [5] of the sought-for electron density distribution. The second possibility is to reduce the degrees of freedom of the problem by expanding the solution in series of orthogonal basis functions. In this approach, different functional forms have been used for interferometer data, i.e. Fourier-Bessel functions [6] or Gaussian functions [7]. However, these basis functions give good results only for specific data sets. No general and physically justifiable

functional form exists for fitting electron density profiles in tokamak plasmas.

In this article, we develop a novel approach to inverting line integrated interferometer data by expanding the sought-for solution into a linear combination of basis functions that are well adapted to the physics determining the transport. The singular value decomposition (SVD) of the Thomson scattering measurements is used to determine these basis functions. In the following, we shall refer to the novel method, which combines the advantages of interferometry with those of Thomson scattering, as the Singular Value Decomposition Inversion (SVD-I) method.

The remainder of the article is organized as follows. In Sec.2, the far infrared interferometer and the Thomson scattering system on the TCV tokamak are described. In Sec.3, MFI and the expansion in basis function methods to perform interferometric inversion are presented. In Sec.4, the SVD-I method is developed and compared to the MFI method using artificial data. Applications to experimental interferometer data discharges in the Tokamak Configuration Variable [8] (TCV) and Joint European Torus [9] (JET) are discussed in Sec.5. Finally, the conclusions are summarized in Sec.7.

The applications presented for the TCV and JET devices are not intended to be an extensive physics study. Rather, the examples and references supplied should be understood as a guided tour in the context of the authors' current research on particle transport. To some degree, the data shown are a revisitation of previous investigations for the purpose of cross-validation. However some of the examples are novel results, which have not been previously published.

2. TCV EXPERIMENTAL SETUP

The TCV device [8] has a major radius $R_0 = 0.89$m, minor radius $a = 0.25$ m and axial magnetic field $B_T \leq 1.54$ T. The TCV vacuum vessel allows for plasmas with elongations up to 2.9. Plasma shaping is performed with 16 independently controlled poloidal field coils. The radio frequency system provides 3MW of EC power for heating and current drive at the second cyclotron harmonic resonance (82.7GHz) using the extraordinary mode [10].

Examples of an extremely elongated and an extremely triangular plasma are shown respectively in Fig.1(b) and (c). The geometry of the magnetic flux surfaces is provided by the equilibrium reconstruction code LIUQE [11]. For practical calculations a grid of 41 equispaced points in the coordinate ρ is used, where we have defined

$$\rho = \sqrt{\frac{\Psi - \Psi_0}{\Psi_a - \Psi_0}} \tag{1}$$

Ψ_0 is the poloidal flux at the magnetic axis and Ψ_a is the poloidal flux at last closed flux surface. In Fig.2, an example of magnetic equilibrium reconstruction is given for the TCV discharge No. 12819. In this figure, the flux surfaces are shown at t = 0.7s and correspond to $\rho = 0.1 \cdot n$, for n = 1, ..., 10.

On TCV, the electron density n_e is obtained by interferometric and Thomson scattering measurements. The far infrared interferometric (FIR) system [3] uses an optically pumped CH_2F_2 laser with a wavelength $\lambda = 214.6\mu$m corresponding to the cutoff density $n_c \approx 2{:}4 \cdot 10^{22}\text{m}^{-3}$. The

plasma is probed along 14 vertical chords of diameter ≈ 20mm in a single poloidal plane as shown in Fig. 1(a). The phase shift $\Delta\phi_i$ between a laser beam passing through the plasma along a straight optical path L_i and a reference beam outside the plasma is measured by a Mach-Zehnder interferometer using heterodyne detection. The signal detectors (InSb hot electron bolometers) provide a frequency response up 100kHz. For all experiments in TCV, the condition $n_e \ll n_c$ holds and the phase shift $\Delta\phi_i$ is proportional to the line integrated electron density

$$\Delta\phi_i = 6.0474 \cdot 10^{-19} \int_{L_i} n_e dl_i,\ i = 1,..., 14 \tag{2}$$

where n_e is expressed in m^{-3}. At the selected wavelength, only minor refraction effects dare present, even at high line averaged densities, $n_e \approx 2.2 \cdot 10^{20}\ m^{-2}$, and the precisionof the measurement is typically $\Delta n_e \approx 5 \cdot 10^{17}\ m^{-2}$.

The TCV Thomson scattering system [12] also provides measurements of electron density profiles. Three nearly co-linear laser beams (wavelength $\lambda = 1.064\ \mu$m, repetition rate to 20Hz.) are injected from the bottom of the TCV vessel at the radial position $R = 0.9$m. The light scattered from 25 sampling volumes, shown in Fig. 1(a), is collected with a spatial resolution of 40mm in the vertical direction and 3mm in the radial and toroidal directions. Sampling intervals down to 0.4ms can be achieved in the so-called 'burst-mode', when the three lasers are triggered close together.

3. METHODS TO INVERT INTERFEROMETRIC DATA

From the mathematical point of view, the calculation of the local electron density profile n_e from line integrated measurements requires the solution of the system of inhomogeneous *Fredholm* equations of the first kind in Eqs.2. This system is always underdetermined, since an infinite number of measurements would be required to solve the system exactly.

On TCV, strongly shaped plasma configurations are produced, so a simple Abel inversion [13] of this system of equations is not of much use. Under these circumstances, additional information is required to obtain a local electron density. Provided that the plasma is not perturbed by strong magnetohydrodynamic (MHD) activity, the electron density is expected to be constant on a toroidally symmetrical magnetic flux surface and depends on the radial flux coordinate ρ alone, i.e. $n_e = n_e(\rho)$.

The supplementary information provided by the flux surfaces is introduced in the system of equations by defining nested pixels, $\rho_i \le \rho \le \rho_{i+1}$, d etermined by the geometry of the magnetic surfaces (shaded pixel in Fig. 2), within which the electron density is considered constant [14], [2]. The electron density is discretized on this grid of nested pixels and the system of integral equations is thus transformed to a system of algebraic equations as

$$(\overline{n}_e)_i = \sum_{k=1,...,n_{pix}} T_{ik}(n_e)_k,\ i = 1,..., n_l \tag{3}$$

which can be arranged in matrix form

$$\bar{\mathbf{n}}_\mathbf{e} = \mathbf{T} \cdot \mathbf{n}_\mathbf{e} \tag{4}$$

The matrix element T_{ik} equals the length of the optical path L_i in pixel k. The line integrated measurements and the density profile form respectively column vectors ne of size nl (the number of line integrated measurements) and ne of size npix (the number of pixels).

In practical situations, a direct inversion of **T** is almost always impossible, either because there are less equations than unknowns ($n_l < n_{pix}$) and therefore the number of solution is infinite or, even if we have $n_l = n_{pix}$, because **T** is badly conditioned.

One way to choose a physically sensible solution is to choose a density profile such that the functional

$$F = x^2 + \alpha R \tag{5}$$

is minimized, where

$$x^2 = (\tilde{\mathbf{T}} \cdot \mathbf{n}_\mathbf{e} - \tilde{\bar{\mathbf{n}}}_\mathbf{e})^T \cdot (\tilde{\mathbf{T}} \cdot \mathbf{n}_\mathbf{e} - \tilde{\bar{\mathbf{n}}}_\mathbf{e}) \tag{6}$$

is the least-square term which provides the consistency of the solution with the line integrated measurements, R is a regularization functional and α is a positive definite parameter. For convenience, we have used the abbreviation $\tilde{T}_{ik} = T_{ik}/\sigma_i$ and $(n_e)_i = (\tilde{\bar{n}}_e)_i/\sigma_i$ where σ_i is the standard deviation of $(\bar{n}_e)_i$.

The parameter α determines the weighting between the goodness of fit (represented by x^2) and the functional R. In the limit $\alpha \to 0$, the solution is determined by x^2 alone as in Eq. 5, while for $\alpha \to \infty$ only the requirements imposed by the functional R determine the solution. The most likely solution is somewhere in between, so one part of the problem is to choose the "correct" value of the regularization parameter α, a second part is to find a solution for this particular value. In practice, provided that the experimental errors σ_i are known suffciently well, the parameter α is determined by minimizing the functional F subject to the constraint $x^2 \approx n_l$, as discussed in details in Refs. [15], [17].

An example of a regularization method used on TCV for soft X-ray tomography [15], [16] and interferometry [7] introduces the Minimum Fisher functional

$$R_{FI} = \int \frac{[n'_e(\rho)^2}{[n_e(\rho)} \, dp \tag{7}$$

where $n'_e(\rho)$ is the derivative of the electron density profile with respect to the radial flux coordinate ρ. An effcient iterative scheme to minimize the functional $F_{FI} = x^2 + \alpha R_{FI}$ has been developed [15] which utilizes the criterion $x^2 \approx n_l$ to determine the "correct" value of the parameter α.

The second possibility to solve the system of Eqs. 3 is to reduce the degrees of freedom by

expanding the local electron density profile into a series of orthogonal functions $w_k(\rho)$ such that

$$n_e(\rho) = \sum_{k=1,\ldots,K_{max}} a_k \cdot w_k(\rho) \tag{8}$$

which can be casted in the matrix form

$$\mathbf{n_e} = \mathbf{W} \cdot \mathbf{a} \tag{9}$$

Using the expansion in Eq. 9, the set of Eq. 3 can be arranged in the matrix form

$$\bar{\mathbf{n}}_\mathbf{e} = \mathbf{T} \cdot \mathbf{W} \cdot \mathbf{a} \tag{10}$$

where the coeffcients **a** are the unknowns of the system. The crucial issue in this approach is the choice of the basis functions $w_k(\rho)$ in Eq. 8 which results in the condition $n_l \geq K_{max}$. Provided that this condition is satisfied, the system of Eqs. 10 becomes an over-determined system for which a least squares solution can be determined by solving the set of normal equations [17]

$$(\mathbf{T} \cdot \mathbf{W})^T \cdot (\mathbf{T} \cdot \mathbf{W}) \cdot \mathbf{a} = (\mathbf{T} \cdot \mathbf{W})^T \cdot \bar{\mathbf{n}}\mathbf{e} \tag{11}$$

In the next section, Thomson scattering measurements of electron density profiles are used to form the basis functions, $w_k(\rho)$, for the expansion of the local electron density profile as in Eq. 8.

4. NEW INVERSION METHOD USING SINGULAR VALUE DECOMPOSITION OF THOMSON SCATTERING DATA

In tokamak transport experiments, the temporal evolution of the electron density can be described by a time-dependent linear combination of spatial eigenfunctions of the operator that governs the dynamical response [18], [19]. Using these particular eigenfunctions, a small number (typically from two to four) of components is usually required to model the evolution of the electron density profile [18], and therefore they constitute well-adapted basis functions to reduce the dimensionality of the system of Eqs. 8. The SVD is particularly effective in identifying these basis functions from spatio-temporal data [20]. The SVD has also been successfully used in the analysis of soft x-ray [19], [21] and magnetic [22] data and in image processing [23]. The basic idea of the SVD-I method to invert interferometric data is to expand the electron density profile in Eq. 8 by using basis functions $w_k(\rho)$ which are obtained from SVD analysis of Thomson scattering data. This choice of basis functions is well adapted to the physics determining the electron density profiles and therefore reduces the number of significant coeffcients, a_k, in Eq. 10 allowing a least-square solution of the inverse problem as in Eq. 11.

In this section, the SVD-I technique is developed, and an example using artificial electron density

data is illustrated. Readers interested in a more rigorous mathematical derivation of the SVD and its fundamental properties can refer for example to Ref. [24].

4.1. DEVELOPMENT OF THE SVD-I METHOD AND COMPARISON TO MFI METHOD

To illustrate the SVD-I method and compare its performance to that of the MFI method, an artificial set of local density data, n_e, that simulates sawtooth activity has been generated (see Sec.5 for details on sawtooth activity). The temporal evolution of the artificial electron density is shown in Fig.3(a,b) for two different radial positions together with two profiles, Fig.3(c), before and after the sawtooth crash. From these artificial data sets the line integrated density, n_e, is calculated using Eq. 11. The transfer matrix **T** is obtained from an actual TCV discharge. Reconstructed local density profiles ne are obtained from both SVD-I and MFI method. The performance of the inversion techniques is thus revealed from a final comparison between n_e and the initial n_e input. Thomson scattering measurements, which are used to form the basis functions, are simulated in this example by choosing a temporal subset of n_e at 15 points. The corresponding times are indicated on Fig.3(b) as vertical dashed lines. In practice, because of the low temporal resolution of the Thomson scattering system, each sample is obtained from a different, but equivalent, sawtooth cycle. Typical samples of Thomson scattering profiles taken over a quasi-stationary discharge include from 50 up to 100 time points for the examples presented in Sec.5 and Sec.6.

To apply the SVD, Thomson scattering electron density profiles $n_e(\rho_i, t_j)$ are arranged in matrix form as follows

$$\mathbf{N_e} = \begin{pmatrix} \hat{n}_e(\rho_1, t_1) & \cdots & \hat{n}_e(\rho_N, t_1) \\ \vdots & \cdots & \vdots \\ \hat{n}_e(\rho_1, t_M) & \cdots & \hat{n}_e(\rho_N, t_M) \end{pmatrix} \tag{12}$$

where M and N are respectively the number of temporal and spatial Thomson scattering samples. On TCV, the standard grid from the magnetic reconstruction code LIUQE assumes $N = 41$ and therefore the inequality $M > N$ usually holds.

The SVD provides a decomposition of the matrix $\mathbf{N_e}$ into three matrices **U, S** and **V** such that

$$\mathbf{Ne} = \mathbf{U} \cdot \mathbf{S} \cdot \mathbf{V}^{\boldsymbol{T}} \tag{13}$$

The matrices **U** and **V** are $M \times N$ and $N \times N$ unitary matrices respectively, i.e. $\mathbf{U} \cdot \mathbf{U}^T = \mathbf{I}$ and $\mathbf{V} \cdot \mathbf{V}^T = \mathbf{I}$. The $N \times N$ matrix **S** is diagonal with positive or zero elements, S_k, which we refer to as the *singular values*. Conventionally, they are ordered in descending order such that $S_1 \geq S_2 \geq \ldots \geq S_N$. The columns of **V** represent spatial eigenmodes $v_k(\rho)$ or *topos*, whereas the columns of **U** can be considered as temporal eigenvectors uk(t) or chronos, where we have adopted the nomenclature of Ref. [19].

In Fig.4, the first three topos are shown together with the power distribution of the topos/chronos couples. As can be seen in this figure, the singular values are strongly ordered and 99.99% of the signal energy, defined as $p_k = S_k^2 \sum_k S_k^2$, is contained in the first three chronos/topos pairs. Here, the local electron density is expanded as in Eq. 8 using the first three topos as the basis functions, $w_k(\rho)$, and a simple least squares solution of Eq. 10 is found. A method to determine the number of components that are needed in the case of experimental data is presented in Sec. 5.

In Figure 5, two artificial electron density profiles are shown (dashed lines), before and after the sawtooth crash, together with reconstructions from artificial line integrated data. Figure 5(a) shows MFI method, Fig. 5(b) the SVD-I method. For the same set of artificial data, the time evolution of the reconstructed electron density using both methods is shown for two different radial positions in Fig. 6(a,b). The time evolution of the artificial electron density is also shown as a dashed line for comparison. In Fig. 6(c), the time evolution of the error in the reconstruction defined as $x^2 = (\mathbf{n_e} - \mathbf{n_e})^T \cdot (\mathbf{n_e} - \mathbf{n_e})$ is shown.

In the case of the peaked profile, a good reconstruction is obtained with both methods for $\rho \leq 0.8$. However, the outermost region of the plasma, $\rho \geq 0.8$, is more accurately reconstructed by the SVD-I method. This is due to the sensitivity of the MFI functional in Eq. 7 to boundary conditions. In the case of the hollow electron density profile, inversions obtained using the SVD-I method are considerably more accurate than the MFI reconstructed profiles. The strength of the SVD-I method is also obvious when we consider the time evolution of the x^2, as can be seen in Fig. 6(c). The smoothing imposed by regularization methods destroys features in the density profiles. By contrast, the SVD-I method utilizes Thomson scattering data and does not impose smoothing of the profile. This allows features to be preserved when they are contained within the set of topos used as computed from Thomson scattering data. It is possible that the MFI method could benefit from utilizing Thomson scattering data in an analogous way but small-scale features may still be smoothed out by nature of the MFI method itself.

It is also worth noting that, due to the small number of computations required, the SVD-I method provides for a fast inversion process. On a PC workstation (Pentium 2, 600MHz, 1GB of RAM) using Matlab 6.0, 10000 time points, similar to the number in a typical TCV discharge, can be inverted in less than 1s for a fixed magnetic equiliubrium. By contrast, inversion of the same set of data would require ≈ 30 minutes using the MFI method.

4.2. THE IMPORTANCE OF ERRORS IN THE THOMSON DATA

For testing the e¨ect of errors in the Thomson scattering measurements, reconstructions were produced from artificial line integrated data with three different levels of noise added on the simulated Thomson measurements: 2.5%, 5% and 10% respectively, the latter representing a rather pessimistic case compared to available experimental data. Figure 7 displays reconstructed peaked and hollow profiles (solid lines) for the different noise levels. Artificial electron density profiles are also shown for comparison (dashed lines). As wo$\underline{\text{u}}$ld be expected, as the level of noise in the Thomson measurements

increases the level of noise in the reconstruction increases as well. However, even for the worst case scenario with 10% noise in the Thomson measurement, the reconstruction still conveys the major features of the electron density profile. We should also note here that the database of the local Thomson scattering profiles from which the basis functions are derived, needs to be rich enough to contain sample profiles which are representative of all phases of the density profile evolution of interest.

5. APPLICATION TO TCV INTERFEROMETRIC DATA

This section, which is not meant to be an extensive physics study, illustrates applications of the SVD-I method to experimental data during sawtooth activity in TCV plasmas.

Sawtooth oscillations, named after the characteristic shape of their soft x-ray time traces, were first observed on the ST tokamak [25] and are present in many tokamak experiments. In ohmically heated plasmas, they consist of periodic relaxations of the central electron temperature and density which develop when the safety factor on axis drops below unity. The sawtooth behavior for normal sawteeth is presented in Fig. 8(a,b) for TCV discharge No. 15279. The temporal evolution of the line integrated electron density, n_e, is shown from a central interferometer chord, Fig. 8(a), and from a chord outside the inversion radius (see definition below), Fig. 8(b). Particle transport is ordinarily characterized by a negative (inward-directed) convective velocity that results in a slow rise (sawtooth ramp) of the line integrated central electron density n_{e0}, Fig. 8(a), and moderately peaked electron density profiles. The sawtooth ramp phase is followed by a rapid drop (sawtooth crash) during which an m/n = 1/1 MHD instability grows (as indicated by soft x-ray tomographic reconstruction [26]) and particles are expelled from the central plasma region defined by $\rho \leq \rho_{inv}$, ρ_{inv} being the inversion radius.

Although sawteeth have been observed and studied in all tokamaks, recent experiments have revealed new peculiar features when electron cyclotron heating (ECH) and electron cyclotron current drive (ECCD) are applied in sawtoothing tokamak discharges. In particular on TCV, with central ECH or ECCD, outward particle convection is observed when a quasi continuous m=n = 1=1 mode is present. This results in inverted sawteeth on the line integrated central electron density and hollow electron density profiles, whilst in the absence thereof, inward convection between successive sawtooth crashes leads to normal sawteeth [26], [27]. The temporal evolution of line integrated interferometric data during inverted sawteeth is presented in Fig. 8(c,d) for TCV discharge No. 18549.

The application of the SVD-I method to real data requires the assessment of the number of components (NC) that are needed in Eq. 8 to expand the electron density profile and whether or not these components can be retrieved from SVD analysis of Thomson scattering data. Using TCV shot No. 18549 as an illustrative example, we discuss a method to determine the NC by comparing the SVD analysis of line integrated interferometric data to the SVD analysis of Thomson scattering data.

To apply the SVD, line integrated data from the 14 interferometer channels $n_e(k, t_j)$ are arranged in matrix form as follows

$$\overline{\mathbf{n}}_{\mathrm{e}} = \begin{pmatrix} \hat{n}_e(1, t_1) & \cdots & \hat{n}_e(14, t_1) \\ \vdots & \cdots & \vdots \\ \hat{n}_e(1, t_P) & \cdots & \hat{n}_e(14, t_P) \end{pmatrix} \tag{14}$$

where P is the number of temporal samples and $k = 1, \ldots, 14$ refers to the channel number as shown in Fig. 1.

In Fig.9(a-d), the first four topos are shown from SVD analysis of the interferometric signals in the time interval of interest $t = 1.499 - 1.53$s in Fig. 8. The power distribution of the singular values S_k, shown in Fig.9(e), reveals four significant components that contain together more than 99.99% of the total signal energy. The first topo, Fig.9(a), corresponding to the largest singular value, represents the contribution to the line integrated data of the spatially-averaged electron density profile. The periodic peaking-flattening of the profile during sawtooth activity is represented by the second topo in Fig.9(b). Analysis of the singular value distribution shows two topos, corresponding to k = 3, 4 whose singular values are close enough to suggest the presence of rotating mode, Fig. 9(c,d). This is confirmed by the corresponding chronos (not shown here) which are oscillating at a frequency of $\approx$ 4kHz and phase shifted by $\pi/2$. This mode is localized at the positions of the interferometer channels $k = 6, 9$, which cross the plasma at opposite sides of the magnetic axis, and therefore exhibits an $m = 1$ structure. This is also confirmed by soft x-ray data as detailed in Furno et al. [27]. Topos/chronos couples corresponding to higher singular values $S_k > 4$ are noise dominated, and no coherent spatial and temporal structures are observed.

From this analysis, we can conclude that the SVD is effcient in separating the dynamics of the sawtooth activity (whose dominant structure is $m = 0$) from the rotation of the $m = 1$ mode. The persistent $m = 1$ mode provides a perturbing asymmetry which is incompatible with the hypothesis of poloidal symmetry underlying the reconstruction. In this case, we filter it out by removing the corresponding singular components ($k = 3, 4$ in Fig.9). This provides the poloidally symmetric component of the line integrated interferometric data that can be inverted using the SVD-I method. When MHD activity is weak or absent, this step of filtering is of course not necessary.

To assess whether or not the SVD of Thomson data can provide the correct basis functions to expand the electron density, we apply the SVD to a set of Thomson scattering profiles measured during the same discharge as detailed in Sec.4.1. In Fig.10(c,d), the first two topos obtained from SVD analysis of 60 Thomson scattering profiles for TCV discharge No. 18549 are shown. The first topo in Fig.10(c), corresponding to the largest singular value, represents the spatially-averaged electron density profile. The second topo in Fig.10(d) represents the periodic flattening-peaking during sawtooth activity. We can therefore conclude that these two topos can be used to expand the electron density in Eq.8 and a least-square solution can be found.

The SVD analysis of line integrated FIR data has been performed for the normal sawtooth case of Fig. 8 resulting in the identification of two components (not shown here) describing the sawtooth dynamics. Also in this case, the topos corresponding to the first two largest singular values, shown

in Fig.10(a,b), as determined by SVD of Thomson scattering measurements provide the correct basis functions to model sawtooth activity.

Here, it is important to note that a basis functions obtained in a particular physical situation should not be expected to reconstruct electron density profiles in a different physical situation. For example, the topo in Fig.10(c) can effectively reconstruct hollow density profiles observed during inverted sawteeth (see discussion below) but it will be inadequate in reconstructing peaked profiles during normal sawtooth activity.

The temporal evolution of local electron density reconstructed using the SVD-I method is shown in Fig.11 for both normal (a,b) and inverted sawteeth (c,d). For the same discharges, electron density profiles are shown in Fig.12 at times indicated by different symbols in Fig.11. In Fig.12(b,d), inverted electron density profiles are compared with profiles as measured by the Thomson scattering system at the same times. Due to the low repetition rate of the Thomson scattering system, only a single profile is measured during the 3 sawtooth periods of Fig.11.

In Fig.13, experimental line integrated data are compared to the line integrated data computed using Eq.4, where ne is the reconstructed profile.

In the normal sawtooth case, n_{e0} increases during the sawtooth ramp and then drops at the sawtooth crash on a fast time scale (typically ≤ 100 *m*s) resulting in a flattening of the electron density profile. After the sawtooth crash, the increase of n_{e0} results from a particle flux in the direction of the density gradient and hence from an inward particle convection, as shown by the temporal evolution of the electron density profile in Fig.12(a,b). In the inverted sawtooth case, the decrease in n_{e0} results from an outward particle flux, which results in a hollowing of the density profile followed by a fast recovery at the sawtooth crash. In both cases, the SVD-I method yields a reconstruction of the electron density profile which reproduces the experimental line integrated data within the measured experimental error bars as shown in Fig.13. The reconstructed profiles are also in excellent agreement ($\leq 5\%$) with the profiles measured by the Thomson scattering at the same times as shown in Fig.12(b,d). This proves that the SVD-I method can be successfully applied to interferometric data in practical situations with experimental errors.

The existence of hollow profiles proves that the normally inward directed particle pinch can be reversed under certain circumstances. Two mechanisms have been proposed to explain this behavior. According to the first [28], the reversal may be due to neoclassical thermodiffusion in the core of the plasma, which is helically displaced by the $m/n = 1/1$ island, making the core region similar to a stellarator. For axisymetrical systems (ideal tokamak), neoclassical thermodiffusion is inward directed (for a monotonic electron temperature profile), while for non-axisymmetrical systems it is outward directed and stronger in magnitude due to the presence of particles trapped in local mirrors [29]. Hollow density profiles of this nature are frequently observed in stellarators. According to the second explanation, derived in axisymmetrical geometry, the outward convection may be due to anomalous thermodiffusion. Outward thermodiffusion leading to hollow density profiles was observed in non-linear collisionless simulations when the electron heating exceeded the ion heating

by a factor of two or more, which is the case in TCV [30]. A recent quasi-linear analysis [31] has shown that this anomalous thermodiffusion is due to trapped electron modes (TEM) and increases in magnitude as the TEM becomemore unstable. The same analysis also suggests that the thermodiffusive outward flux may not be suffcient to overcome the curvature driven flux, which is always inward for positive shear discharges. Since these calculations were made in axisymmetrical geometry, their relevance to hollow density profiles correlated with m/n = 1/1 islands is unclear. Although the theory of anomalous transport in non-axisymmetrical systems is less developed, there is no reason to believe that anomalous convection should not occur in those systems as well. The explanation of density flattening by anomalous outward thermodiffusion does appear to apply to the reduction of the density gradients in the confinement zone (outside the q = 1 radius and arguably axisymmetrical even in the presence of a m/n = 1/1 island) of TCV, which is observed in the presence of powerful central ECH irrespective of the presence or absence of m = 1, n = 1 islands[32], [33]. The phenomenon of density profile flattening has also been observed on ASDEX Upgrade in high density plasmas in the presence of Ion Cyclotron Resonance Heating (ICRH) [34], although it was interpreted as solely due in increased electron particle diffusivity brought about by the central heating, in the presence of a constant or weakened Ware pinch. An analogous mechanism is observed to occur on AUG in high density plasmas with central ECRH [31]. Figure 14 shows an example of the SVD-I method applied to an ELMy, sawtoothing H-mode in TCV. The figure shows reconstructed traces near the edge (ρ = 0.9), at ρ = 0.6 and on-axis. The occurrences of ELMs, inferred from a D_α signal, are marked by broken vertical lines. For a period of ≈ 1ms at the ELM crash, a strongly asymmetrical perturbation is observed, which prevents a meaningful reconstruction. The corresponding periods are left blank in the traces of Fig.14. We found that the line integral of the reconstructed profiles for the chords closest the edge is poor in H- mode. Having ascertained that this is not an effect of beam refraction in the pedestal region, where gradients are strong, we realized that this chord passes within less than the Thomson scattering radial resolution (≈ 3cm after mapping) of the Last Close Flux Surface (LCFS). Hence the SVD analysis of Thomson scattering profiles is unable to generate basis functions that allow the H-mode pedestal region to be adequately represented and reconstructed. Consequently we have omitted these chords in the reconstructions of Fig.14. We have compared the results of the SVD-I to those from Thomson scattering for a wide range of sawtoothing Ohmic L-mode discharges in TCV. These discharges were presented previously in an investigation of density profile behavior, which showed that the broadness $< n_e > / n_{e0}$ of the electron density profiles is directly related to the peaking of the current density profile, irrespective of plasma shape, average density and collisionality (see e.g. Fig.1B in Ref.[33]). The same data are shown in Fig.15 for Thomson scattering (dots) and for SVD-I (triangles) demonstrating good agreement. As previously shown [32], the scaling of electron density peaking with current density peaking is in agreement with Turbulent Equipartition Theory (TEP) [35]. The fact that good reconstructions are obtained for a modest number of topos (2-4 depending on circumstances), suggests that a smaller number of interferometer chords than available on TCV may be sufficient.

We tested the idea by performing reconstructions with reduced sets of approximately evenly spaced chords and found that the quality of the reconstructions remains virtually unchanged down to as few as 5 or 6 chords (for 4 topos), as shown in Fig. 16 for a broad and for a peaked density profile. ELMy H-modes are also reconstructed satisfactorily with 5 chords using 3 topos, but for 4 topos, 6 chords are often required. The robustness of the reconstruction at low chord numbers is an important advantage for larger fusion devices, such as JET, where access restrictions limit the number of interferometer lines.

6. APPLICATION OF SVD-I TO JET DISCHARGES

We have applied the SVD-I to a set of several hundred discharges in L- and H-mode in JET. JET is equipped with an 8 channel system [14] and a LIDAR Thomson Scattering system [36]. The pedestal region is not resolved by the 4Hz core LIDAR system, which has a relatively modest resolution of some 12cm for the JET low field side minor radius of typically 85cm. JET has a higher resolution edge Thomson scattering system, but it currently has a lower repetition rate (1Hz) and is not always available, which is why we haven't included it in the present analysis. For the same reasons as in TCV, we have excluded edge chords, which are nearly tangent to the LCFS, and the chord passing through the X-point, which can pick up a significant contribution from outside the LCFS, leaving 5 chords for the reconstructions. The SVD-I was applied to study the behavior of the density profile in a series of Lower Hybrid Current Driven (LHCD) discharges presented previously [40]. These plasmas all had the same plasma current $Ip = 1.3$MA, corresponding to $q_{95} = 8$. They were also free from sawteeth and other MHD activity and had $q_0 > 1$. Applying a range of powers of off-axis LHCD up to 3.6MW, the magnetic shear in the core was reduced and eventually reversed. The width of the density profile followed the width of the current profile as $< ne > /ne_0 \approx 2/3 \cdot l_i^{-1}$, where the internal inductance l_i is a measure of the peaking of the current profile, in qualitative agreement with predictions from TEP [35] and its counterpart in fluid theory, the curvature pinch [30]. These discharges had no MHD activity, which is why reconstructions with two (as in the figure) or three topos provide the same result within 2%. In Ref.[37], the analysis of the interferometer signals was based on a three parameter functional fit, made available to the JET community as a standard [38].

The present analysis has shown that the SVD-I produces inversions that reproduce the raw interferometer signals more accurately than the functional fit. The result is that the density profiles are somewhat more peaked than those quoted in Ref.[37]. Figure 17 can directly be compared to Fig. 13 in Ref. [37]. However, all parametric dependencies remain qualitatively similar, in particular the dependence on l_i, the independence of the peaking on electron temperature gradient length L_{Te} and on the theoretically important effective collisionality, relevant for Ion Temperature Gradient (ITG) and TEM instabilities, which is defined as

$$\nu_{eff} = \nu_{ei}/\omega_{De} \approx 3(m_i/m_e)^{1/2} \epsilon^{3/2} \nu^*_{ei}/q \qquad (15)$$

where ν_{ei} is the electron ion collision frequency, ν_{ei} is the electron collisionality familiar from neoclassical theory, ω_{De} is the curvature drift frequency and ϵ the local aspect ratio. The approximation introduced above and used in this paper stems from the assumption $k_\theta \rho \approx 1/3$ for the fastest growing poloidal mode number $k_\theta \rho$, which is supported by fluid and kinetic microstability calculations (ρ is the ion Larmor radius). These discharges have been analyzed with respect to microinstabilities with the gyrokinetic code GS2 [39], using gradients at mid-radius as inputs. The main result is that the sign of the mode frequency, which indicates the nature (ITG or TEM) of the dominant instability, is very sensitive to input parameters. This stresses the importance of accurate profile measurements for meaningful stability calculations. We interpret the sensitivity of the mode frequency as an indication that the discharges are in a mixed ITG/TEM regime, where thermodiffusion is expected to be weak, consistently with the absence of an L_{Te} dependence. The behavior of H-modes is in stark contrast to the L-mode, Fig. 18, with a clear collisionality dependence and no l_i dependence, except for $\nu_{eff} < 0.3$ [40]. Although a scaling with both l_i and ν_{eff} [41] is expected from theory, it is presently not understood why no ν_{eff} dependence is observed in L-mode and why an l_i dependence is only apparent at low collisionality in H-mode, although it appears to be linked to the fact that H-modes at medium and high collisionality are clearly in the ITG domain. Once the ν_{eff} dependence is acknowledged, there are no further dependencies on $< n_e >$, nor on $P_{ICRH}=P_{AUX}$, $P_{NBI}=P_{AUX}$, L_{Te}, L_{Ti}, β_N or ρ^*.

Figure 18 confirms the collisionality dependence of the density peaking observed on ASDEX Upgrade [41] and extends it to lower collisionalities. The vertical broken line indicates the collisionality expected for the ITER reference H-mode. $n_{e0}/ < n_e >$ is slightly less (by $\approx 7\%$) at $\nu_{eff} \approx 0.2$ in JET than in ASDEX Upgrade when the evaluation of ν_{eff} is based on a flat Z_{eff} derived from visible Bremsstrahlung. However, JET and ASDEX Upgrade results agree when lower and hollow Z_{eff} profiles measured by charge exchange spectroscopy are used. The agreement between the two different size devices suggests the possibility of an extrapolation to ITER. Assuming similar conditions (no significant α particle heating), we expect that the peaking factor on ITER for $\nu_{eff} \approx 0.1$ will be $n_{e0}/ < n_e > \approx 1.6 \pm 0.2$, as at JET, corresponding to $R/L_{ne} \simeq 4 \pm 1.3$ at mid-radius. However, the power density available for electron heating in the core of JET is relatively modest and therefore not representative of an ignited plasma. Density peaking in ITER is likely to be reduced from the level observed in JET by the strong α heating, which is expected to drive TEM unstable, producing an outward thermodiffusive convection [31].

SUMMARY

The SVD-I method combines the high bandwidth of interferometer systems with the spatial accuracy of Thomson scattering. It uses SVD of temporally sparse local electron density profile measurements from a Thomson scattering system in the same or equivalent plasmas to determine a set of orthogonal basis functions which is well adapted to the physical processes under investigation. The sought-for density profile is expanded into series of a small number of these functions and a solution is calculated

by using a simple least-square fit method. An SVD analysis of line integrated interferometer measurements allows the determination of the number of components that are needed to reproduce the evolution of the density profile in a particular situation. This information is used for optimizing the number of local basis functions to include in the inversion. We have shown that the SVD-I method is more accurate and faster than a regularization method for reconstructing density gradients and hollow profiles. The SVD-I method has been successfully applied to invert interferometric measurements from TCV plasmas during normal and inverted sawteeth. In the former case, with Ohmic and low power ECH, the density profiles are consistent with TEP predictions, i.e. the peaking of the density profiles is directly related to the peaking of the current profiles, irrespective of plasma shape and average collisionality. Departures from TEP occur with high power ECH and ECCD, leading to flatter and sometimes hollow (when a $m/n = 1/1$ island is present) density profiles. The existence of hollow density profiles proves that the normally inward directed particle pinch can be reversed under certain circumstances. The observed pinch reversal in the presence of a ($m/n = 1/1$) island is consistent with neoclassical predictions of reversed thermodiffusion in the core of a helically deformed plasma.

The robustness of the SVD-I method, even in the presence of a small number of line-integrated measurements (down to as few as 5 or 6 chords), allows the inversion of interferometric data from JET plasmas. We applied the SVD-I method to a set of MHD-free, L-mode discharges previously analyzed using a three parameter functional fit [38]. All parametric dependencies remain qualitatively similar between the two methods. In particular, we found that $< n_e > /n_{e0}$ is independent from both the electron temperature gradient length L_{Te} and the collisionality ν_{eff}. Yet, the SVD-I method provides inverted profiles which are more peaked and reproduce the interferometric raw data more accurately than functional fit profiles.

Using the SVD-I method, we studied the dependence of the density peaking on the effective collisionality in H-mode discharges in JET. The main result is that we observed the same collisionality dependence of density peaking as in ASDEX Upgrade [41] and extended it to a lower collisionality regime as shown in Fig. 18.

ACKNOWLEDGEMENTS

The authors wish to thank the entire TCV team for their valuable help. Discussions with J.B. Lister, S. Sardy and E. Hemsing are gratefully acknowledged. The authors also acknowledge support from the *Fonds National Suisse de la Recherche Scientifique*.

REFERENCES

[1]. K.L. Chiang *et al*., Rev. Sci. Instrum. 68, 894 (1997).

[2]. J.P.T. Koponen and O. Dumbrajs, Rev. Sci. Instrum. 68, 4038 (1997).

[3]. S. Barry, Ph.D. thesis, National University of Ireland, Cork, CRPP report LRP 638/99 (1999), see http://crppwww.epfl.ch/archives/1999/lrp1999/lrp 638 hq.pdf.

[4]. G. Braithwaite *et al.* , Rev. Sci. Instrum. 60, 2825 (1989).

[5]. B.R. Frieden, J. Mod. Opt. 35, 1297 (1988).
[6]. H. Ruan and B. Wan, International Journal of Infrared and Millimiter Waves 21, 1973 (2000).
[7]. I. Furno, Ph.D. thesis No. 2434, , EPFL, Lausanne, CRPP report LRP 703/01 (2001), see http://crppwww.epfl.ch/archives/2001/lrp2001/lrp 703 01 hq.pdf.
[8]. F. Hofmann *et al*., Plasma Phys. Control. Fusion 36, B277 (1994).
[9]. J. Pamıela *et al*., Nucl. Fusion 43, 1540 (2003).
[10]. T. P. Goodman *et al*., in *Proceedings of the 19th Symp. on Fusion Technology, Lisbon, (North-Holland, Amsterdam 1997)* (1996), vol. 1, p. 565.
[11]. F. Hofmann *et al*., Nucl. Fusion 20, 1871 (1988).
[12]. R. Behn *et al*., in *Proc. of the 7th Int. Symp. Laser Aided Plasma Diagnostics, Fukuoka* (2002), p. 392.
[13]. I. Hutchinson, *Principles of plasma diagnostics* (IOP Publishing Ltd 2000, 1987).
[14]. J. H. Williamson and D. E. Evans, IEEE Trans. Plasma Sci. PS-10, 82 (1982).
[15]. M. Anton *et al*., Plasma Phys. Control. Fusion 38, 1849 (1996).
[16]. J. Mlynar *et al*., Plasma Phys. Control. Fusion 45, 169 (2003).
[17]. W. H. Press, *Numerical recipes in Fortran* (Cambridge University Press, 1992).
[18]. J.M. Moret and Tore Supra, Nucl. Fusion 32, 1241 (1992).
[19]. T. Dudok de Wit *et al*., Phys. Plasmas 1, 3288 (1994).
[20]. G. H. Golub, *Matrix Computations* (Baltimore . Johns Hopkins University Press, 1996).
[21]. C. Nardone, Plasma Phys. Control. Fusion 34, 1447 (1992).
[22]. J. S. Kim, Plasma Phys. Control. Fusion 41, 1399 (1999).
[23]. T. S. Huang, Appl. Opt. 14, 2213 (1975).
[24]. J. Stoer and R. Bulirsh, *Introduction to numerical analysis* (Springer, New York, 1980).
[25]. S. V. Goeler, Phys. Rev. Letters 33, 1201 (1974).
[26]. I. Furno *et al*., Nucl. Fusion 41, 403 (2001).
[27]. I. Furno *et al*., Phys. Plasmas 10, 2422 (2003).
[28]. H. Weisen *et al*., Nucl. Fusion 41, 1227 (2001).
[29]. L. M. Kovrizhnykh, Nucl. Fusion 24, 851 (1984).
[30]. X. Garbet *et al*., Phys. Rev. Letters 91, 03500 (2003).
[31]. C. Angioni *et al*., Nucl. Fusion 44, 807 (2004).
[32]. H. Weisen, Nucl. Fusion 42, 136 (2002).
[33]. A. Zabolotsky *et al*., Plasma Phys. Control. Fusion 45, 735 (2003).
[34]. J. Stober *et al*., Nucl. Fusion 41, 1535 (2001).
[35]. D. Baker and M. Rosenbluth, Phys. Plasmas 5, 2936 (1998).
[36]. H. Saltzmann *et al*., Rev. Sci. Instrum. 59, 1451 (1988).
[37]. H. Weisen *et al*., Plasma Phys. Control. Fusion 46, 751 (2004).
[38]. J.P. Christiansen, J. Comput. Phys. 73, 85 (1987).
[39]. M. Kotschenreuter *et al*., Comp. Phys. Commun. 88, 128 (1995).
[40]. H. Weisen *et al*., 31*st EPS Conference on Plasma Physics, London*, P1-146 (2004).
[41]. C. Angioni *et al*., Phys. Rev. Letters 90, 205003 (2003).

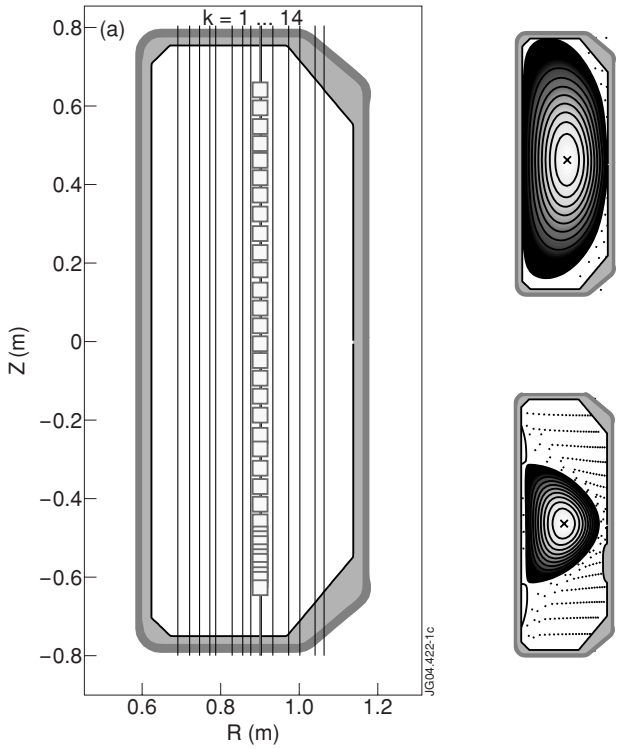

Figure 1: Far Infrared Interferometer on TCV. (a) Geometrical arrangement of the 14 laser beams probing the plasma. Shown as squares are also the 25 scattering volumes of the TCV Thomson system. (b,c) Two extreme plasma shapes in TCV.

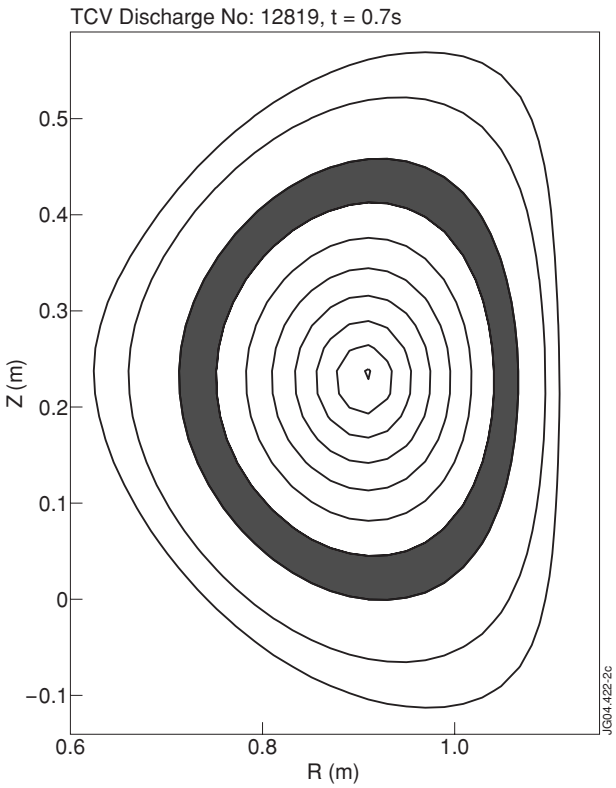

Figure 2: Nested pixels corresponding to TCV magnetic flux surfaces as calculated by the equilibrium code LIUQE. Shown are magnetic flux surfaces corresponding to $\rho = 0.1 \leq n$ for n = 1,…, 10. The pixel corresponding to $0.7 \leq 1/2 \leq 0.8$ is shown in gray. The electron density is assumed constant in each pixel.

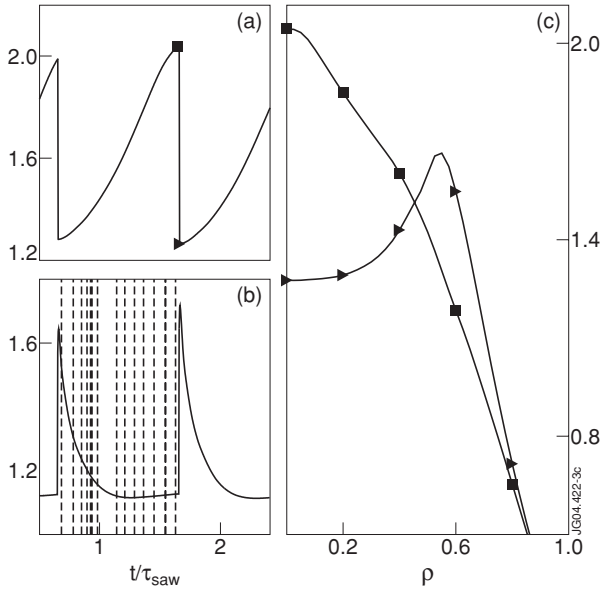

Figure 3: Artificial local electron density measurements simulating sawtooth activity in the plasma. Time evolution of the electron density at different radial positions: (a) on axis, (b) just outside the inversion radius, (c) electron density profiles at different times indicated by different symbols in (a). Vertical dashed lines in (b) indicate times used to build the subset of Thomson profiles to form the basis functions.

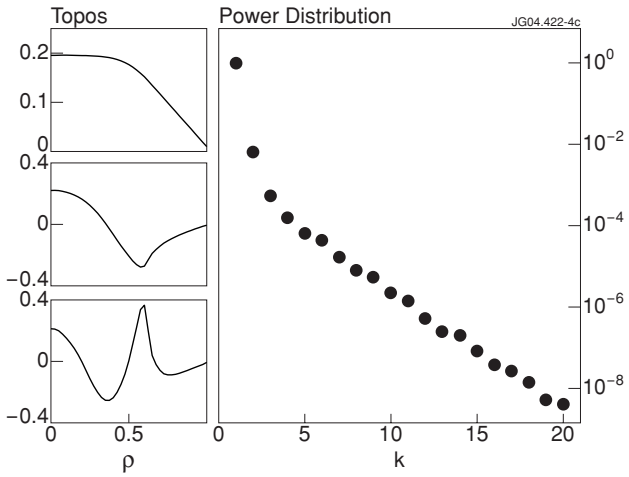

Figure 4: Singular value decomposition of simulated Thomson scattering data. Thomson data are simulated by choosing a temporal subset of the artificial electron density data in Fig.3. The first three topos are shown on the left together with the power distribution of the first twenty topo/chrono couples. 99.99% of the signal energy is stored in the first three topos.

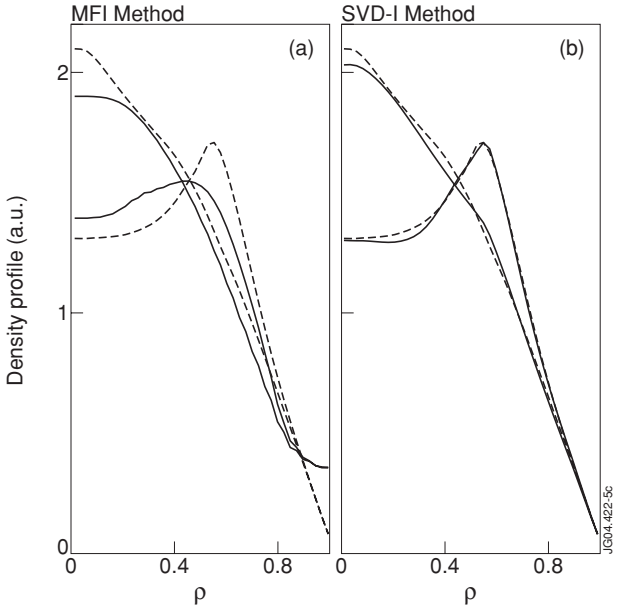

Figure 5: Inverted electron density profiles (solid lines) from the simulated density profiles (dashed lines) also shown in Fig.3. The MFI and SVD methods are compared for peaked and hollow profiles.

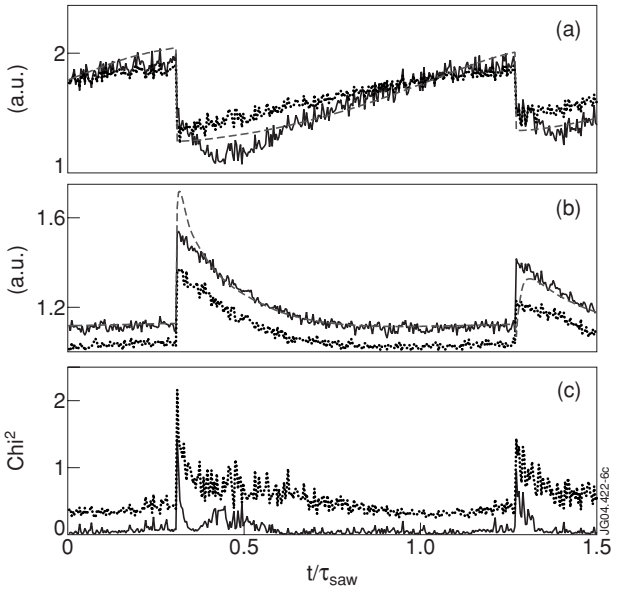

Figure 6: Artificial electron densities. Time evolution of the electron density is shown as a dashed line, inversion of line integrated measurement using the MFI method is shown as a light solid line, and inversion using the SVD-I method is shown as a dark solid line for different radial positions: (a) on axis, and (b) just outside the inversion radius. Error of inversion methods in ρ space is shown in (c) as a function of time.

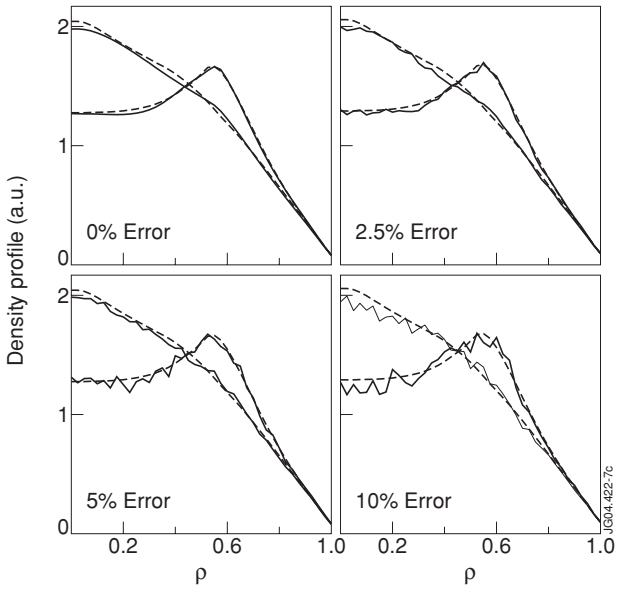

Figure 7: Inverted electron density profiles (solid lines) using the SVD-I method from artificial line integrated data. Different levels of noise are added on Thomson scattering profiles used to calculate the basis functions. The artificial electron density profiles (dashed lines) are also shown for comparison.

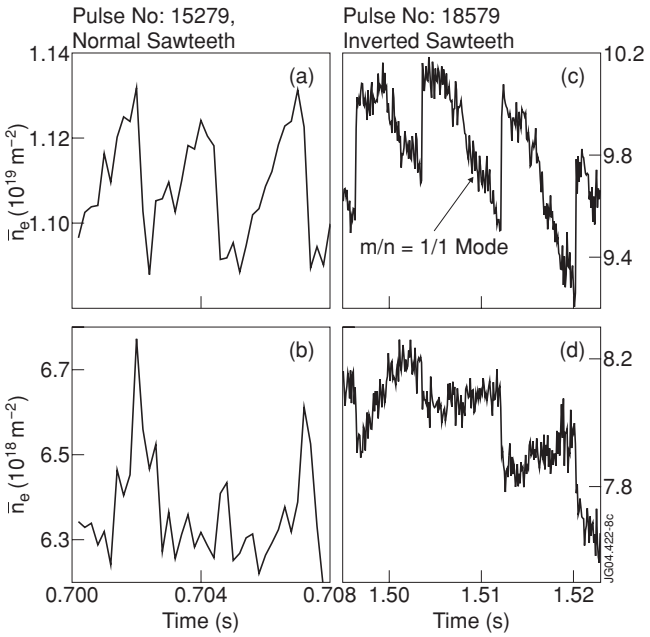

Figure 8: Temporal evolution of line-integrated interferometric measurements during normal (a,b) and inverted (c,d) sawteeth. Shown are measurements along a central chord (a,c) and a chord just outside the sawtooth inversion radius (b,d).

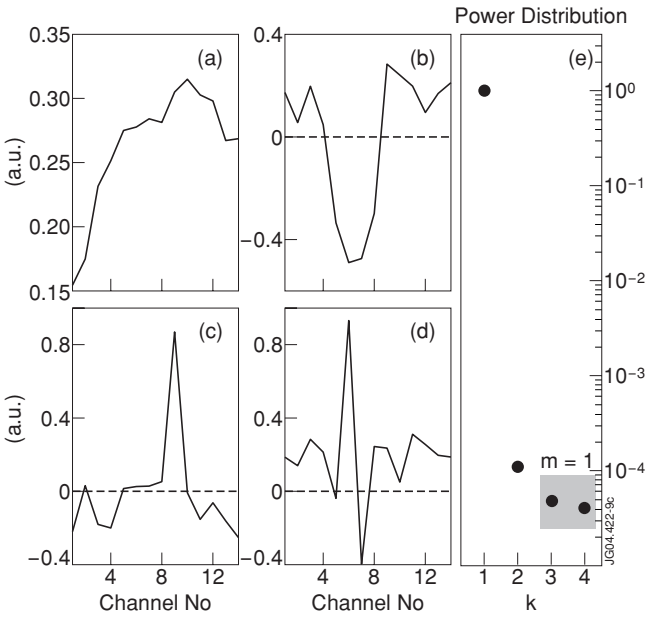

Figure 9: SVD analysis of the 14 line integrated interferometric signals during inverted sawteeth in the time window shown in Fig.8. Shown are the topos corresponding to the four largest singular values (a-d) together with the distribution of the singular values (e). Two almost identical singular values, k = 3; 4, suggest the presence of a rotating mode.

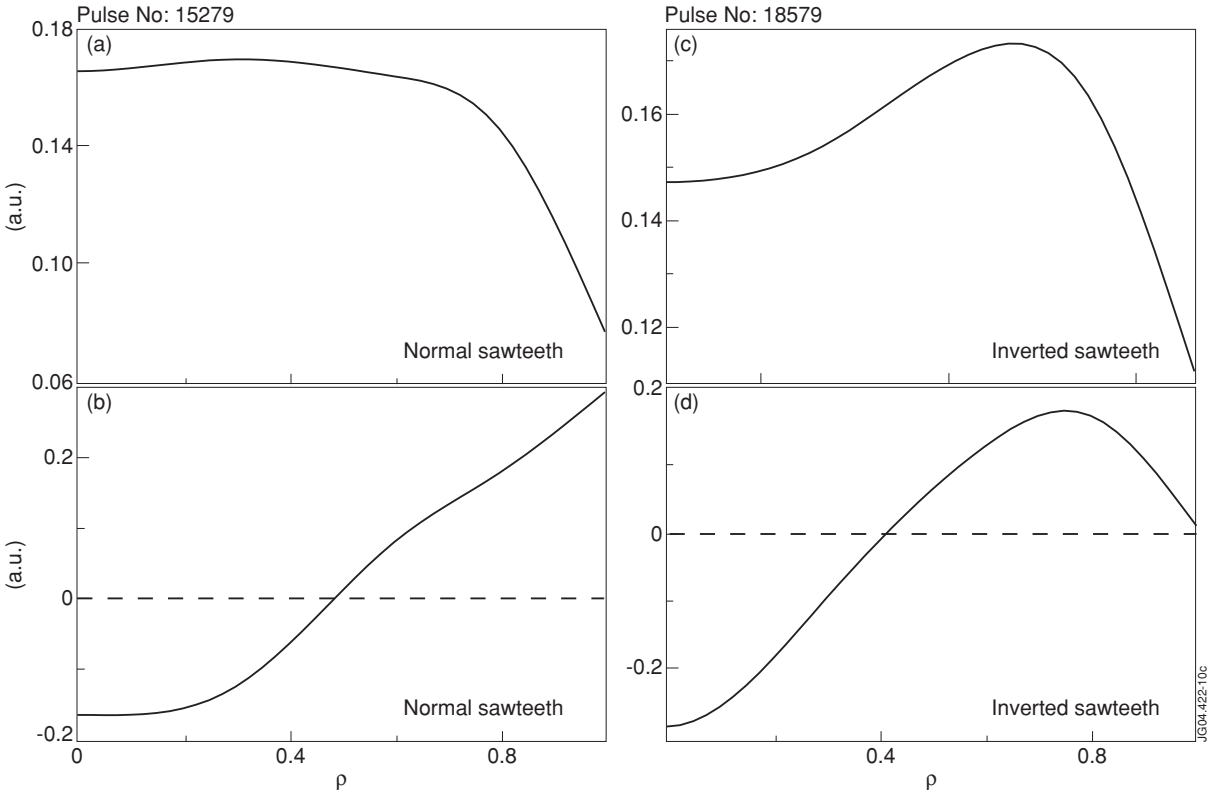

Figure 10: SVD analysis of Thomson scattering measurements for TCV discharge No. 15279 (a,b) and discharge No. 18549 (c,d). Shown are the topos corresponding to the two largest singular values.

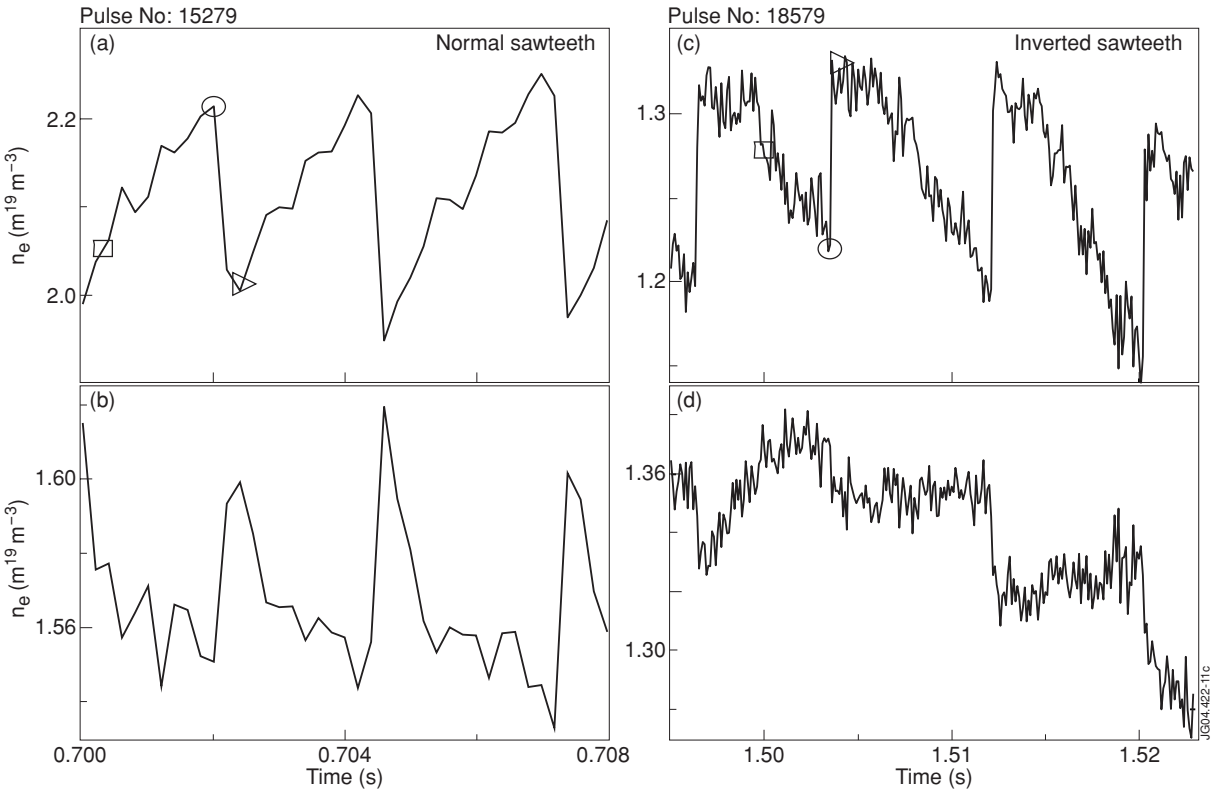

Figure 11: Temporal evolution of local electron density reconstructed using the SVD method at different radial positions during both normal and inverted sawteeth for two TCV discharges shown in Fig.8. (a,c) On-axis; (b,d) Just outside the sawtooth inversion radius. Different symbols (square, triangle, circle) indicate times corresponding to the electron density profiles in Fig.12.

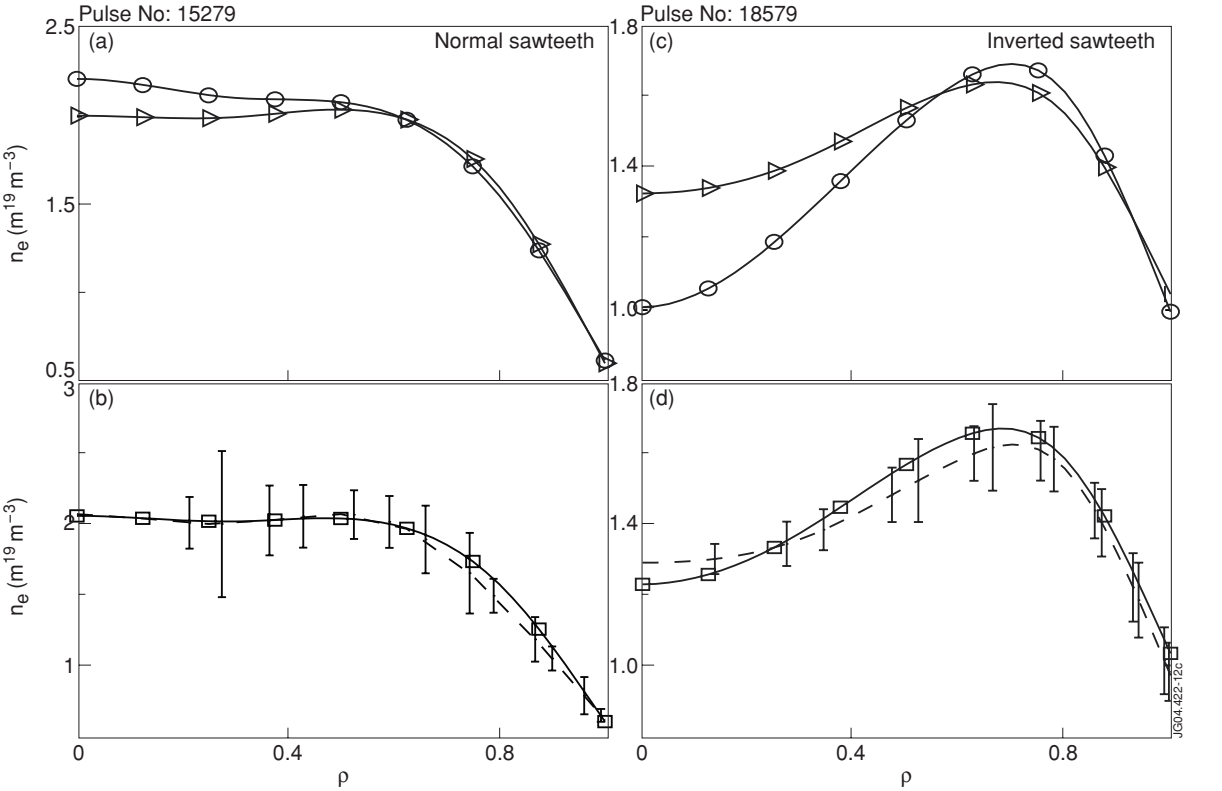

Figure 12: Reconstructed electron density profiles using the SVD method during normal and inverted sawteeth. Times correspond to different symbols in Fig.11. (a,c) Profiles before (circle symbols) and after (triangle symbols) the sawtooth crash. (b,d) Profiles during the sawtooth ramp (square symbols) are compared with profiles (dashed line) as measured by the Thomson scattering system at the same times.

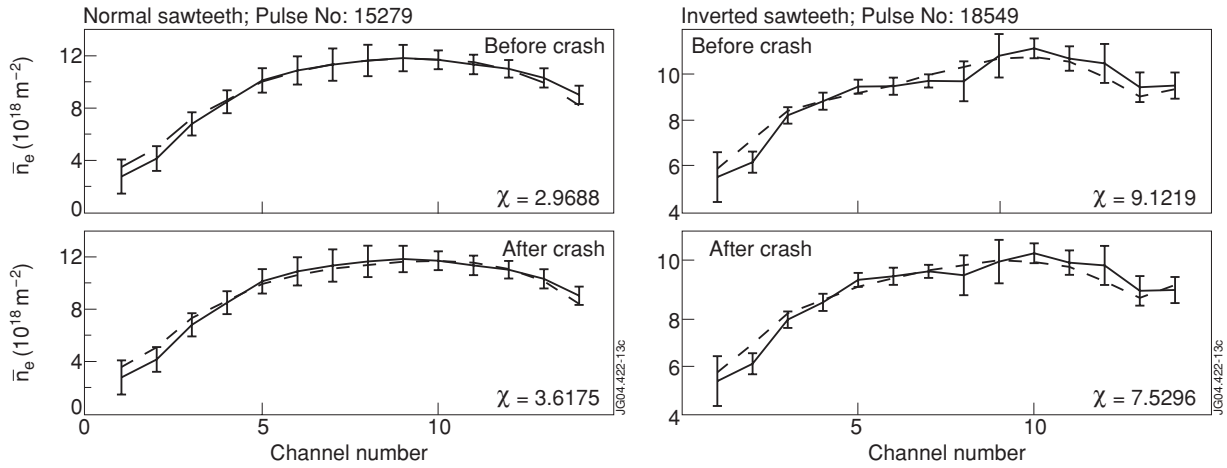

Figure 13: Comparison of line integrated experimental data (solid line) with line integrated data (dotted line) as calculated from reconstructed profiles using Eq. 4.

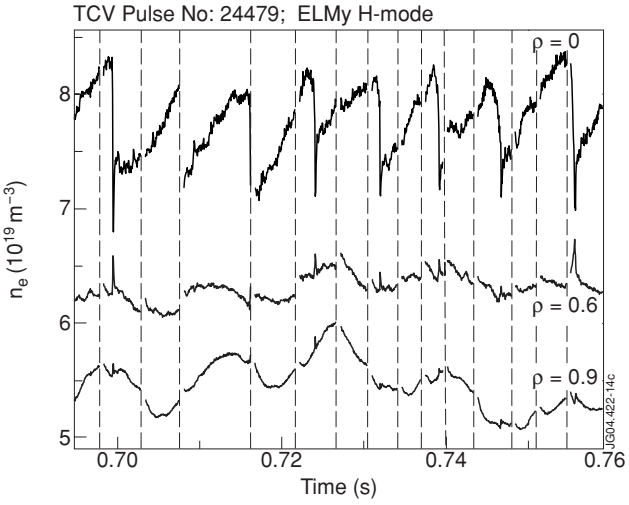

Figure 14.: Time evolution of reconstructed density at three positions in an ELMy H-mode using 4 topos and 12 chords. Vertical lines indicate ELMs. The density at ρ = 0.9 has been scaled by a factor of 1.6 to avoid overlapping.

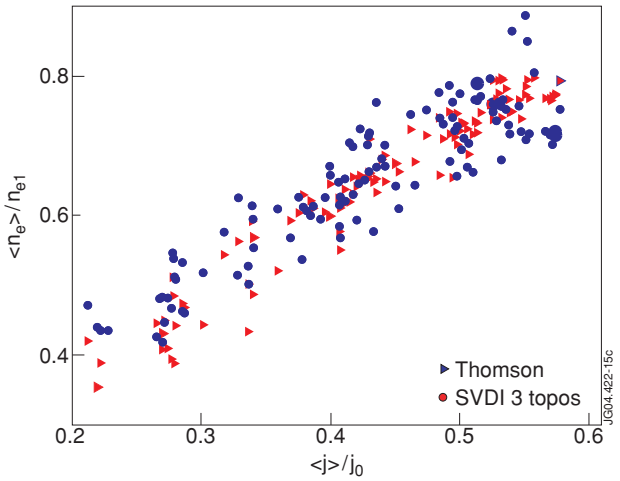

Figure 15: Dependence of density profile width on current profile peaking in sawtoothing Ohmic L-mode discharges in TCV. Dots: using only Thomson scattering. Triangles: using SVD-I with 3 topos.

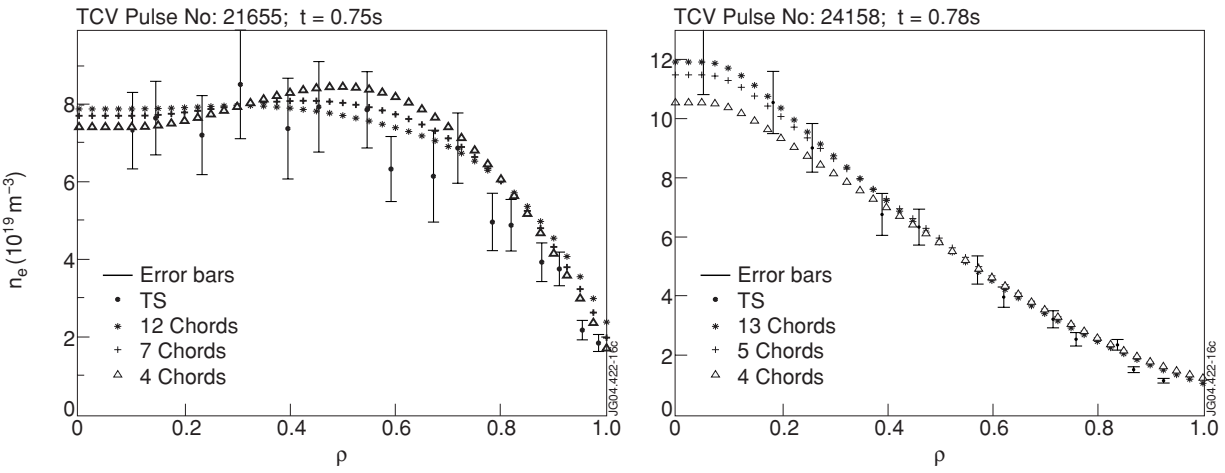

Figure 16: Reconstruction of a density profiles using a reduced number of interferometer lines a) broad profile with q_{95} = 2:4, (4 topos used) b) peaked profile with q_{95} = 4:5 (2 topos used).

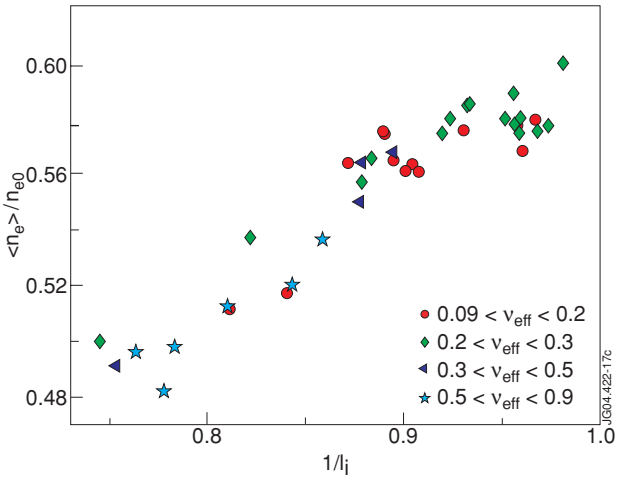

Figure 17: Dependence of density profile width on internal inductance in MHD-free LHCD L-mode discharges in JET. Symbols indicate different classes of effective collisionality.

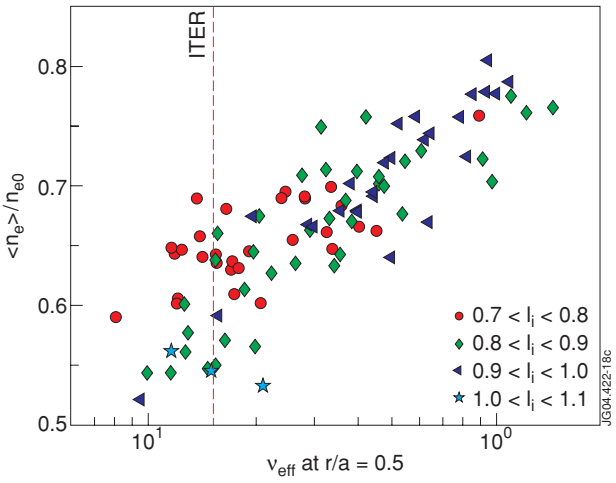

Figure 18: Dependence of density profile width on effective collisionality in ELMy H-mode discharges in JET. Symbols indicate different classes of internal inductance. A vertical line is drawn at the effective collisionality expected for the ITER reference H-mode.